Observations of the Roots of Plasma Bubbles: Are they sometimes foamy?

Charles Lougheed Bennett[1]

[1]Lawrence Livermore National Laboratory (retired)

May 16, 2023

1

Observations of the Roots of Plasma Bubbles: Are They Sometimes Foamy?

Charles L. Bennett[1]

[1]Lawrence Livermore National Laboratory (retired).

Corresponding author: Charles Bennett (Charlie_Bennett@comcast.net)

Key Points:

- Dispersionless, highly attenuated, lightning generated electromagnetic waves are observed in the lower ionosphere

- The propagation of these electromagnetic waves has characteristics of acoustic wave propagation through two-phase foams

- Such foamy plasma bubbles may cover approximately 80% of the bottomside of the equatorial nightside ionosphere.

14 **Abstract**

15 Dramatic irregularities in the plasma density of the ionosphere, first discovered by their effects
16 on radio wave propagation in 1938, and despite decades of investigation, still remain puzzling.
17 Their deleterious effects on radio wave communication, satellite command and control, GPS
18 navigation are serious enough to strongly motivate better understanding of their nature. Many
19 aspects of such irregularities are now understood, but the mechanism(s) of their formation and
20 their detailed nature remain a topic of great interest. In this work, detailed time resolved
21 measurements of lightning generated waves show dispersionless, strongly attenuated propagation
22 with substantial propagation delays. These characteristics of the electromagnetic wave
23 propagation in the two-phase bubble/non-bubble ionosphere parallel the characteristics of
24 acoustic wave propagation through two-phase liquid/vapor foams; and this motivates the
25 suggestion that the bottomside layer of the ionosphere may sometimes be foamy.

26 **Plain Language Summary**

27 Just as ocean waves breaking at the interface between sea and land produce copious bubbles and
28 foam, recent satellite data suggests a similar phenomenon at the interface between neutral
29 atmosphere and the charged plasma of the ionosphere. Lightning generated electromagnetic
30 waves passing through the lower ionosphere observed by low altitude satellites are found to have
31 the same characteristics as acoustic waves passing through foamy water. This hypothetical foam
32 in the lower ionosphere apparently strongly absorbs radio waves and seems to prevent most such
33 waves from escaping the foam to pass through to the upper ionosphere.

34 **1 Introduction**

35   This article is a sequel to (Bennett, 2023), that describes a novel method for the
36 observation and analysis of the *roots* of equatorial plasma bubbles (EPBs). Most of the details in
37 (Bennett, 2023) will not be repeated here, but a brief summary is presented in the following
38 section 2.

39   EPBs are localized density depletions (sometimes by over four orders of magnitude
40 relative to the surrounding plasma) in the nighttime equatorial ionosphere (Heelis, 2004; Kil &
41 Heelis, 1998; Woodman & Hoz, 1976). The literature on EPBs is vast and spans nearly a
42 century. Nowadays there is increasing motivation to understand such bubbles and their
43 detrimental affects on radio communications, especially satellite communications, for which
44 "loss of lock" events can be precipitated by their presence. Another detrimental effect is the
45 disruption of signals from the Global Navigation Satellite System so important to modern
46 society. Numerous reviews of the development of the experimental and theoretical understanding
47 of plasma bubbles are available (e.g. Balan et al., 2018; De Michelis et al., 2021; Huba, 2023;
48 Kelley et al., 2011; Makela & Otsuka, 2012; Woodman, 2009).

49   It is generally accepted that the lower density of plasma bubbles relative to their
50 surroundings causes them to rise in a turbulent process giving rise to plumelike features in radar
51 observations (e.g. Abdu et al., 2012; Hysell et al., 2005; Kelley et al., 2011; Kudeki &
52 Bhttacharyya, 1999; Narayanan et al., 2014; Patra et al., 2005; Tsunoda, 1983; Yokoyama et al.,
53 2011). Plasma bubbles may also be detected as emission depletion bands in optical observations,
54 (e.g., Immel et al., 2003; Kil et al., 2004; Makela & Kelley, 2003; Makela et al., 2006; Makela &
55 Miller, 2008; Martinis et al., 2003; Mendillo & Baumgardner, 1982; Pimenta et al., 2003;
56 Shiokawa et al., 2004). Animations of sequences of optical images, such as those in Makela and

57 Miller (2008) most clearly and dramatically show plasma bubbles emerging from low altitudes
58 with subsequent rising and Eastward drifting. Such animations not only show apparent turbulent
59 structures emerging from regions of depleted emission, but also show apparently non-turbulent
60 depleted emission regions extending continuously below the turbulent regions towards the base
61 of the ionosphere. In the present article the term *roots* of plasma bubbles refers to density
62 depletions that extend *contiguously* to the base of the ionosphere that aren't necessarily turbulent.
63 It is beyond the scope of this article to explain exactly how these density depletions are formed.

64 Initial observations and most early investigations of plasma bubbles involved so-called
65 "spread F" phenomena, in which radar pulses of a given frequency, rather than reflecting from
66 distinct ionospheric layers corresponding to distinct altitudes of reflection were observed to
67 return from a spread out region of altitudes (Woodman, 2009). As such radar reflections require
68 the presence of ionospheric density irregularities at the scale of the radar wavelength,
69 conventional spread F phenomena would not be seen for non turbulent roots of plasma bubbles.

70 Woodman (2009) states "We implicitly assume that there is a cascade mechanism as
71 proposed by Haerendel (1973) from the larger to the smaller scale, but we do not know exactly
72 how this takes place." Woodman (2009) further states "The current state of the theory is that
73 high frequency drift instabilities can explain the shortest wavelengths, up to ~1 m and the low
74 frequency waves longer than 10 m, but no existing theory can explain the waves around 3 m, i.e.,
75 the strong echoes that Jicarmarca sees!"

76 Kelley (2011) states "How structure can be transferred from 1000 km to 1 m is still a bit
77 of a mystery. Since there is linear growth in the power law regime, it is not because of an inertial
78 cascade" and "Much remains to be done before the electrodynamics and coupling processes in
79 this region during solar minimum conditions are fully understood."

80 To this day, the formation of the initial density depletions evidently required to "seed"
81 larger scale turbulent fluctuations responsible for the greatest degradations of radio
82 communications are not fully understood (Chou et al., 2022; De Michelis et al., 2022; Huba,
83 2023; Kil et al., 2022).

84 The remainder of this paper is organized as follows: Section **2** provides a summary of the
85 earlier (Bennett, 2023) paper involving the detailed description of the data sources and analysis
86 methods relevant to the current work. The main new results in the current work involve the
87 detailed wavevector analysis of both dispersed (i.e. whistlers) and unusually low dispersion
88 waves. In addition, previously unnoticed "precursors" to the ususually low dispersion whaves are
89 identified and described. Normally dispersed waves are discussed in section **3**. In section **4**
90 unusually low dispersion waves are discussed. Section **5** presents a physical model for "foamy"
91 plasma. The various observations in (Bennett, 2023) and the new observations in the present
92 paper are interpreted in terms of this model. Section **6** provides further discussion and
93 conclusions.

94

2 Highlights of Earlier Work and New Observations

96 In (Bennett, 2023) I suggested that the roots of plasma bubbles might sometimes be
97 foamy. This suggestion was made based on the propagation characteristics of lightning generated
98 (LG) waves passing through such roots and in analogy to the propagation of acoustic waves
99 through mixed liquid/gas phase foamy media. A specific model of the propagation of

100 electromagnetic waves through such "plasma foam" at the bottom of the ionosphere will be
101 discussed in Section **5**.

102   In Figure **1**, a slightly expanded region of that shown in Figure 11 of (Bennett, 2023), the
103 electric field signals observed by the EMFISIS instruments on the Van Allen Probe (VAP)
104 satellite at 2.5°S 154.6°W altitude 239 km from a single lightning flash located at 9.2°N 84.8°W,
105 comprising four strokes, are shown. In Figures **1b**, **1d** and **1f**, the temporal variations of the
106 electric field components E_u, E_v and E_w along the three axes, U, V and W of the spinning VAP
107 satellite are shown. The W axis is spin aligned and approximately vertical here. Figures **1a**, **1c**
108 and **1e** display scalograms for the three electric field components computed using a continuous
109 wavelet transform (CWT) as described in (Bennett, 2023). Scalograms display the time
110 dependence of the frequency components of a waveform and feature higher temporal resolution
111 at higher frequencies following the cone of influence (COI) function. An example of the COI
112 function centered at the time of the second pulse is shown in Figure **1e** by the white curved
113 dashed line. An impulsive disturbance at a single time sample in the electric field would produce
114 a scalogram peak with the shape of the COI. The COI also indicates how data outside the time
115 period used in the CWT may affect the scalograms. The COI of the boundary effects is shown as
116 a curved black dashed line in **1a**, **1c** and **1d**. Scalogram values at frequencies below the boundary
117 COI are unreliable. For example, in **1a** and **1c**, at the start of the time period, the greenish region
118 below the COI is a boundary artifact.

119   The appearance times of the four peaks seen in Figure **1f**, are delayed by 20, 31, 30 and 7
120 ms as indicated above Figure **1e** relative to the arrival times of LG pulses at the subsatellite
121 location. The curve shown in Figure **1g** is the sum of the waveforms from the Nickolaenko et al.
122 (2004) model using parameters for the stroke intensities and arc distances from the subsatellite
123 position to the stroke location detected by the World Wide Lightning Locator Network
124 (WWLLN) over the time period shown. WWLLN is a global Very Low Frequency (VLF; 3-
125 30kHz) lightning location system capable of finding the radiated energy, time and location of
126 individual lighting strokes with ~10 km spatial accuracy, ~10 µs temporal accuracy and ~90%
127 efficiency for high peak current strokes (Abarca et al., 2010; Holzworth et al., 2019; Hutchins et
128 al., 2012; Jacobson et al., 2006; Rodger et al., 2006). Red vertical lines in Figures **1b**, **1d** and **1f**
129 mark the three peaks in the composite model electric field function shown in Figure **1g**. The
130 (Nickolaenko et al., 2004) model propagation speed of 245 km/s accurately matches the
131 observed travel speed 245±5 km/s for ELF pulses observed at ground level by the World ELF
132 Radiolocation Array (WERA), as discussed by (Bennett, 2023) and shown in Figure 10 of that
133 article. The propagation speed of LG pulses through the Earth Ionosphere waveguide (EIWG) is
134 primarily a function of the altitude of the EIWG upper boundary (EIWGUB) as discussed in
135 (Golkowski et al., 2018). All of the VAP data in this article were acquired near local midnight,
136 so that most of the stronger LG pulses travelled entirely through regions with higher EIWGUB
137 altitudes. The second of the four pulses seen in Figure **1f** was detected in the Geostationary
138 Lightning Mapper (GLM) (Bateman et al., 2020; Goodman et al., 2013; Rudlosky et al., 2019)
139 data, but not in the WWLLN data.

140   A feature of the data shown in Figure **1c** that was not noticed by (Bennett, 2023) is the
141 presence of two "Precursor" streaks most clearly seen in the E_v scalograms near 10 kHz. These
142 precursors first appear approximately 4 ms after the red vertical lines in Figure **1a-1f**. A similar
143 precursor is only marginally apparent preceding the fourth peak and no significant precursor
144 appears before the second pulse in Figure **1f**. Examination of other VAP data bursts reveals that

145 such precursors often do appear, albeit only in a minority of the cases for which clear, well
146 identified LG peaks are seen in the scalograms. In numerous other cases, such precursors are
147 found very well correlated with the subsatellite arrival time of EMPs predicted using the
148 Nickolaenko et al. (2004) model and WWLLN measured times and locations. In the first nine
149 figures in the Supplemental materials **S1**, 22 distinct examples of precursors may be seen.

150 Another significant example involving multiple strokes from a single lightning flash is
151 shown in Figure **2**. In this case, a single flash at 12.7°N 152.8°E comprising three WWLLN
152 strokes occurring in rapid succession produces three precursors and three bipolar pulses in the
153 electric field components. The bipolar pulses are narrowest in the E_v component and broadest in
154 the E_u component. The precursors in this case appear strongest in the E_u component, are
155 significant in the E_v component but lost in the noise in the E_w component. The relatively broad
156 temporal extent of the precursors suggests that they may be a novel form of spread F, but seen at
157 frequencies far below radar frequency and in terms of direct propagation delay rather than as
158 reflected pulses. Validation of the assumed 245 km/s group velocity for propagation through the
159 EIWG in this case is validated by the WERA data for these LG pulses shown in the last three
160 figures in the Supplemental materials.

161 Despite the substantial propagation delays for the LG events seen in Figures **1f** and **2d**,
162 no significant increase in the widths of the pulses (relative to the model pulses in Figures **1g** and
163 **2g**) from the propagation through the EIWG from the location of the lightning flash to the
164 subsatellite point was seen. This dispersionless propagation of LG EMPs through the lower
165 ionosphere exemplified by Figures **1 & 2** is in stark contrast to the characteristics of normal
166 whistlers. In the following section **3**, the detailed behavior of normal whistlers is quantitatively
167 described. In section **4**, unusual dispersion events are discussed. A possible physical explanation
168 of both the "spread F like" precursors and the delayed bipolar dispersionless pulses will be
169 discussed in Section **5**.

170

171 **3 Wave Vector Analysis for Normal Whistler Events**

172 3.1 Normal Two Fluid Plasma Dispersion Relations

173 In (Bennett, 2023) it was empirically found, for propagation angles θ relative to the local
174 magnetic field not close to ±90°, that both the phase and group velocities versus frequency of
175 fast magnetosonic "whistler" waves for frequencies above the relevant ion cyclotron frequency
176 and below the electron cyclotron frequency have a square root dependence on frequency
177 insensitive to ion mass. Numerically the group velocity vs. frequency is approximately

178

$$V_{group} = 189 \; \frac{km}{s\sqrt{Hz}} \; \sqrt{\frac{75 \, mm^{-3}}{N_e} \frac{B}{31 \, \mu T}} \; \sqrt{f} \; , \tag{1}$$

180

181 while the phase velocity is approximately

182

183
$$V_{phase} = 112 \frac{km}{s\sqrt{Hz}} \sqrt{\frac{75\ mm^{-3}}{N_e} \frac{B}{31\ \mu T}} \sqrt{f\cos(\theta)} \quad . \tag{2}$$

184

185   These general and characteristic features of the classical whistler portion of the dispersion
186   relations (De Jonghe & Keppens, 2021b) are seen in observational data for whistlers in "normal"
187   plasma regions, but are *violated* in regions of unusual dispersion.

188

189   3.2 Normal Dispersion Relation Observations

190   Figure **3** of the present work shows the scalograms from a 1.6 second portion of the
191   scalograms shown in Figure **5** of (Bennett, 2023). The overall travel time, including the
192   propagation time through the EIWG to the subsatellite location, ΔT_0, followed by the passage
193   upwards through the ionosphere to the satellite detectors is given by the integral of the inverse
194   group velocity over the path length as

195

196
$$\Delta T = \int \frac{ds}{V_{group}(s)} = \Delta T_0 + DC/\sqrt{f} \quad . \tag{3}$$

197

198   In the equality on the right hand side of expression (3), the dispersion constant (DC)
199   value implicitly represents the integral over all variations along the path *through the ionosphere*
200   of the factors in expression (1). Superimposed over the scalograms in Figure **3**, the white vertical
201   dashed line shows the arrival time of an LG pulse at a time ΔT_0 after the WWLLN observed
202   stroke time. The three curved red dashed lines show three dispersion curves having DC values of
203   0.1, 12 and 24 $s\sqrt{Hz}$, and having the same arrival time at the subsatellite location as the white
204   dispersionless case. For DC values much less than 0.1 $s\sqrt{Hz}$, *normal* whistlers appear effectively
205   dispersionless, arriving at a time ΔT_0 after the associated lightning stroke.

206   3.3 Wavevector Analysis of Normal Dispersion Observations

207   Figure **4** of the present work shows a wave vector analysis using the amplitudes along the
208   four superimposed dispersion curves indicated by dashed lines in Figure **3**. At each frequency
209   and time along the dispersion curves having DC values indicated in the column titles for Figures
210   **4a**, **4f**, **4k** and **4p**, the complex amplitudes of the scalograms for the electric and magnetic fields
211   are used to compute the Poynting vector

212

213
$$\boldsymbol{S}(f) = \boldsymbol{E}(f) \times \boldsymbol{B}^*(f) \quad , \tag{4}$$

214

215   and the unit Poynting vector

216

217
$$\widehat{\boldsymbol{S}}(f) = \boldsymbol{S}(f) / |\boldsymbol{S}(f)| \quad . \tag{5}$$

218

219   The absolute values of the scalar product of the unit Poynting vector with each of the unit
220   vectors in the mean field aligned (MFA) coordinate system described in (Min et al., 2017; Ritter
221   et al., 2013) as a fuction of frequency are shown in the top three rows of Figure **4**. The MFA
222   coordinate labels here (μ, ϕ, and ν) follow the notation of Min et al. (2017). The scalar products
223   along the local magnetic field are indicated by |S•μ| in the ordinate label in **4a**. The scalar
224   products along the magnetic East direction in the horizontal plane are indicated by |S•ϕ| in the
225   ordinate label in **4c**. The scalar products along the direction orthogonal to the first two
226   directions, approximately vertical in the equatorial region, are indicated by |S•ν| in the ordinate
227   label in **4b**. In **4d**, **4i**, **4n** and **4s**, the absolute value of the electric and magnetic field scalogram
228   components are shown as a function of frequency. The random phase approximation (RPA) for
229   the phase velocity as a function of frequency is computed according to the method described by
230   (Bennett, 2023) from the complex scalogram amplitudes along each of the four dispersion curves
231   shown in Figure **3**, and is plotted in Figure **4e, 4j, 4o** and **4t**.

232   Expression 2 is used to estimate the propagation angles θ in Figure **4e, 4j, 4o** and **4t** by
233   fitting the high frequency behavior of the four cases. These estimated angles are shown in blue in
234   the last row of Figure **4** and the phase velocity vs. frequency variation of expression 2 is shown
235   by the green line in Figure **4e, 4j, 4o** and **4t** above the oxygen cyclotron frequency. Below the
236   oxygen cyclotron frequency the phase velocity is shown by the horizontal section of the green
237   line at its long wavelength limit assuming the plasma is predominantly O^+ ions.

238   Since the "noise" of other contributions to the scalogram amplitudes along the four
239   dispersion curves is not negligible, significant fluctuations are seen in the estimated Poynting
240   vector projections displayed in the top three rows of Figure **4**. Even so, it seems the direction of
241   the *energy* flow for the low dispersion whistler and its echos are traveling in approximately
242   consistent directions, in contrast to the apparent variation in the direction of the *wavevector*
243   suggested in the last row of Figure **4**. The sign of the energy propagation direction is irrelevant in
244   the plots of the absolute values of the energy propagation direction cosines shown in the top
245   three rows of Figure **4**. This whistler and its echos are travelling obliquely in the MFA
246   coordinate system, with unit Poynting vector projections of approximately 0.8, 0.5 and 0.4 along
247   the μ (magnetic field B), ν (~vertical), and ϕ (magnetic East) directions.

248

249

250   Even though the dispersion constant (DC) values are dramatically different for the four
251   cases displayed in Figure **4**, the RPA estimated phase velocities for all four cases are not so
252   different, and are consistent with slightly different cos(θ) angular factors. The reason for the
253   great differences between the DC values is that they represent integrated totals of the dispersion
254   over the full distance (in the last two cases including the echoing path) from source to detector.
255   This sensitivity of the DC values to the integrated dispersion along the full path from source to
256   detection was extensively exploited and discussed in (Bennett, 2023). In contrast, the four
257   dispersiveness coefficients (50, 50, 80 & 112) in the legends in **4e**, **4j**, **4o** and **4t** are local
258   measurements, characteristic of the conditions of the ionosphere at the location of the detectors,
259   rather than an integral measure along the full propagation path.

260   Finally, some measure of the fidelity of the RPA estimates for phase velocity can be
261   judged by the degree to which the scalograms are found to have significant values above the

262 ambient "noise". For example, for the Bu component displayed in **3a**, scalogram amplitudes for
263 frequencies below 100 Hz appear to decrease to the level of the "background" amplitudes
264 primarily associated with the population of slow magnetosonic waves discussed in (Bennett,
265 2023). Other components are similarly "lost" in the background noise at a variety of frequency
266 levels. As a guide for the interpretation of which frequencies have meaningful values for both the
267 direction projections shown in the top three rows, and the phase velocities shown in the bottom
268 row of Figure **4**, the cyclotron frequencies for Oxygen and Hydrogen are shown by the white and
269 magenta dashed lines in Figure **3** and cyan and magenta dashed lines in Figure **4** in order to more
270 readily identify regions having significant amplitudes for all six electromagnetic components.

4 Wave Vector Analysis for Unusual Disperion Events

271

4.1 A Region of Unusual Dispersion

272

273 Figure **5** of the present work shows the scalograms from a single data burst acquired
274 shortly before the burst scalograms shown in Figure 9 of (Bennett, 2023). In this figure, the
275 arrival times of EMPs from every lightning strike detected by the WWLLN are shown by the
276 vertical dashed white lines. Not a single normally dispersed whistler is observed during this data
277 burst. This data has the character described in (Bennett, 2023) for periods that the Van Allen
278 probe is passing through the root of a plasma bubble contiguously connected to the EIWG.
279 Specifically,

280 1. the dispersion constant (DC) values become anamolously small relative to the
281 estimate from the international reference ionosphere (IRI) model for the time and
282 location of the satellite,

283 2. it is observed that the "spikes" in the scalograms corresponding to anamolously small
284 DC values do not extend much above 1 kHz, in contrast to normal, very low
285 dispersion cases outside plasma bubble regions that extend all the way to the Nyquist
286 frequency as seen in Figure **3**,

287 3. the electric field fluctuations become enhanced by several orders of magnitude
288 relative to typical values seen just before or just after entering the bubble region,

289 4. the magnetic field fluctuations are not especially enhanced relative to typical values
290 outside the bubble region,

291 5. where both electric and magnetic field fluctuations are significant relative to their
292 surroundings, the estimated phase velocity is orders of magnitude faster than expected
293 relative to the IRI model estimate.

294 The last three of these points are clearly seen in the spectra, as shown by comparison of the
295 fourth column relative to the first or third columns in Figure 7 of Bennett (2023).

296 In the first portion of the data shown in Figure **5** prior to the identified "Period of
297 Interest", there are a great number of dispersionless spikes seen in the electric field scalograms,
298 most of which do not have corresponding well isolated spikes substantially above the ambient
299 clutter noise from the ubiquitous slow magnetosonic waves (Bennett, 2023) in the magnetic field
300 scalograms, so that a wavevector analysis of the sort described for Figure **4** is not feasible
301 because of the high degree of "clutter noise". The number of spikes is much greater than the
302 number of detected WWLLN strokes during this period. Furthermore, the timing of the WWLLN

303   stroke arrivals do not line up well with the strong dispersionless spikes in the VAP data. Since
304   the wavevector analysis shown above in Figure **4** relies on having scalogram amplitudes for all
305   six electric and magnetic field components that are reasonably stronger than the surrounding
306   "noise" of other waves, the region indicated by the bracket with arrows labeled "Period of
307   Interest" has been chosen for further wavevector analysis because of the availability of
308   significant dispersionless spikes in the magnetic field scalograms. This region is also of interest
309   as it appears to be at the edge of a plasma bubble, since the dispersionless spikes are suddenly
310   not seen after this period.

311

312   4.2 Scalograms from A Region of Unusual Dispersion and the Cone of Influence

313   Figure **6** shows in more detail scalograms of the three magnetic and electric field
314   components for the bracketed region indicated in Figure **5**. Superposed on the scalograms are
315   eight white vertical dashed lines labeled #1 - #8 chosen to pass through peaks in either the
316   magnetic or electric scalograms. The four dashed red vertical lines are drawn at the predicted
317   arrival times of LG waves at the subsatellite location, using the WWLLN measured locations and
318   strike times assuming a propagation speed through the EIWG of 245 km/s. For each of the four
319   WWLLN detected waves, the angular distance from the subsatellite point to the WWLLN
320   determined strike location is indicated in **6f** by the blue text numbers.

321

322

323

324   The noisiness of the following wavevector analysis for propagation direction and phase
325   velocity may be attributed to the variability in the contributions from the numerous other waves
326   present at the times chosen for analysis. The cone of influence (COI) shown by the curved red
327   dashed lines superimposed over the scalogram plots in Figure **6** shows the boundary COI, as
328   described in section 2 above. The COI also represents the "confusion time range" over which
329   other waves contribute to the scalogram amplitudes associated with a given peak. For example,
330   the strongest spike in the electric field scalograms, labeled #6, spreads more broadly in time at
331   lower frequencies just as does the COI shown by the curved white dashed line in **6d**, **6e** and **6f**
332   centered at peak #6.

333

334   4.8 Foamy Behavior of Unusual Dispersion Regions

335   The wavevector analysis shown in Figure **7** for cases labeled #3, #4, #5 and #8 in Figure
336   **6** displays an unusual phase velocity distribution. At frequencies below the local oxygen
337   cyclotron frequency, the RPA estimated phase velocity is approximately 30 Mm/s for all four
338   cases. For cases #3 and #5, above the oxygen cyclotron frequency the RPA phase velocity drops
339   to approximately 2 Mm/s and *is approximately constant*. In contrast, cases #4 and #8 in the 2nd
340   and 4th columns, appear to alternate between 2 Mm/s and 30 Mm/s regions.
341   The results displayed in Figures **7e** and **7o** are in stark contrast to the normal variation of
342   phase velocity as a function of frequency seen in Figures **4e**, **4j**, **4o** and **4t**. In the Figure **7e** and
343   **7o** plots the constancy of the phase velocity above the relevant local cyclotron frequency,
344   Oxygen in this case, cannot be explained by any normal IRI model. In general, the local plasma
345   dispersiveness produces a phase velocity increasing as the square root of the frequency, as in

346   expression **2**. Evidence that the phase velocity for these waves is not merely locally
347   dispersionless, but also nearly dispersionless along their full path through the ionosphere to the
348   satellite is simply that the appearance in the scalograms such as in Figures **1** or **2** is of purely
349   vertical spikes with negligible indication of dispersion beyond the Nickolaenko et al. (2004)
350   model, *despite substantial overall propagation delays*.
351   The ionospheric length of the propagation path followed by LG waves cannot be less than
352   a purely vertical path of approximately 190 km from the EIWGUB to the satellite, and thus the
353   propagation delays of 12 and 25 ms for events #1 & #2 as indicated in Figure **6a**, correspond to
354   mean speeds no less than 16 and 8 Mm/s. Although the magnetic field scalogram spikes in
355   Figure **6a**, **6b** & **6c** for events #1 & #2 have such high "clutter noise" that a wavevector analysis
356   of the type shown in figure **7** is unreliable, these speeds at least do have the same order of
357   magnitude as the RPA estimates shown in the last row of plots in Figure **7** for peaks #3, #4, #5
358   and #8.
359

5 Propagation of Magnetohydrodynamic Waves Through A Model Plasma Foam

361   Even in the absence of magnetic fields or ionization, the propagation of acoustic waves
362   through foamy mixtures of gaseous and liquid phases is complex, as discussed for example in
363   (Benjelloun & Ghidaglia, 2021; Elias et al., 2020; Pierre et al., 2013). Remarkably, prior to
364   experimental confirmation, in 1941 Wood, on the basis of physical arguments, argued that the
365   speed of sound in a mixture of two fluids would be that of a single fluid having density equal to
366   the volumetric mean density of the two fluids, and compressibility equal to the volumetric mean
367   compressibility. In a mixture of air bubbles in water for example, the speed of sound, according
368   to Wood's law, may be orders of magnitude slower than the speed of sound in either water or air.
369   This is because the mixture density is dominated by the water fraction, while the mixture
370   compressibility is dominated by the air fraction. It has been found (Elias et al., 2020) that
371   Wood's law indeed reliably predicts the velocity of sound in most liquid foams *when the bubbles*
372   *are much smaller than the acoustic wavelength*.

373   Isolated small air bubbles in water are most likely to be nearly spherical. By contrast, low
374   density plasma bubbles embedded in higher density plasma at the bottom of the ionosphere are
375   expected to extend along local magnetic field lines. In the model of a small region of the lower
376   ionosphere illustrated in Figure **8**, "normal" plasma is represented by the gold colored material
377   while very low plasma density depletion bubbles are represented by voids. In this model, the
378   bubbles are drawn with circular shapes in the plane perpendicular to **B**, and with a random
379   assortment of positions and diameters. The presence of the magnetic field produces a sensitive
380   dependence on the direction of propagation of magnetohydrodynamic (MHD) waves relative to
381   **B**. With the local speed of sound much less than the Alfven speed, magnetosonic waves tend to
382   separate into fast waves moving nearly perpendicular to **B** and slow waves moving nearly
383   parallel to **B** (Jackson, 1975). As the waves discussed here are fast, I consider waves moving
384   exactly perpendicular to **B**. Such waves propagate with a speed dependant on the sum of
385   hydrostatic and magnetic pressures.

386   In the plane perpendicular to B, the section of "foamy" plasma shown has dimensions of
387   a single wavelength in both the East/West and Up/Down directions. With the approximation that
388   the compressibility of normal density plasma is much less than the compressibility of low density
389   bubbles, the speed of fast magnetosonic waves in the mixture becomes much less than the speed

390 in either normal density plasma or low density bubbles. This speed is also a sensitive function of
391 the bubble volumetric fraction, and may vary erratically from one sample to the next. The wide
392 variety of propagation delays seen in Figures **1** and **2** can be explained by this erratic variation.

393 For wavelengths shorter than the smallest of the plasma bubble radii in this model, MHD
394 waves would tend to propagate only within the circular cross section "waveguides" bounded by
395 the high conductivity plasma "walls", as either (Jackson, 1975) transverse electric or transverse
396 magnetic modes. With a variety of bubble diameters and plasma densities within the bubbles, the
397 group velocities of short wavelength modes passing through these waveguides would also be
398 variable. The spread in the arrival times of high frequency, short wavelength waves seen in the
399 form of "precursors" in Figures **1** and **2** can be explained by this process. Because of the low
400 plasma density within these effective waveguides, the highest propagation speed may be quite
401 high, and the earliest precursor signals may appear immediately after the arrival of LG pulses at
402 the subsatellite location, as seen in the numerous examples in Figures **1** and **2** and the
403 supplemental figures.

404 Finally, the frequency spread of the "precursors" is sometimes limited to a narrow range
405 (e.g. from just below to just above 10 kHz in the Figure **1c** case), but more often extends over a
406 wider frequency range (e.g. from about 1 kHz to 20 kHz in the Figure **2a** case). Examination of
407 the various examples of "precursors" in the first nine supplemental figures reveals that the
408 frequency spread of the "precursors" is relatively consistent over the brief periods shown in these
409 figures. Examination of the numerous examples shown in Figures **1** and **2** and the supplemental
410 figures further reveals that the unusual, nearly dispersionless spikes in the scalograms do not
411 usually extend much above a few kHz. From the disperion relations for fast magnetosonic waves
412 travelling in a primarily O^+ plasma, as shown in Figure **1d** of Bennett (2023), this frequency
413 corresponds to wavelengths of a few km. Both the lower frequency limit of the extent of the
414 "precursors" and the upper frequency limit of the scalogram spikes suggest that the mean spacing
415 of the bubbles in Figure **8** is typically on the order of magnitude of 1 km. This model then
416 naturally explains the lower frequency bound of the "precursors" and the upper frequency bound
417 on the dispersionless scalogram spikes.

6 Discussion and Conclusions

419 Another characteristic of "foamy" behavior is strong attenuation. This effect is more
420 difficult to prove directly with the Van Allen probe observations. In some rare cases, such as
421 those displayed in Figures **1** and **2**, multiple intense strokes of lightning are seen emerging from
422 a single location that may be identified with individual LG pulses measured by the Van Allen
423 probe detectors. With nearly identical paths traversed from source to detector, the correlation
424 between propagation delay and attenuation may be made. However, because of the inherent
425 variability in foamy plasma model illustrated in Figure **8**, the uncertainties in these
426 measurements within a single burst of data are quite large. For the data shown in Figure **1**, it is
427 found that an attenuation of 49±22% corresponds to a propagation delay of 19±12 ms, while for
428 the data shown in Figure **2**, an attenuation of 1±0.7% corresponds to a propagation delay of
429 131±5 ms. These values plotted in Figure **9** provide suggestive evidence for strong attenuation of
430 fast magnetosonic waves with propagation distance through foamy plasma. A more indirect
431 manifestation of the strong attenuation of LG waves passing through such hypothetical foamy
432 plasma is the fact that most lightning strokes do not produce detectable whistler events in the
433 Van Allen probe data.

434 In (Zheng et al., 2015) a search for coincident detections of LG events by the Van Allen
435 probe satellites and the WWLLN was made. For the subset of lightning strikes within 18° of the
436 subsatellite location, only 15.3% of the strikes were detected by the Van Allen probe
437 instruments. The relatively low 15% coincidence rate found in this study could be explained by
438 the presence of underlying plasma bubble foam covering approximately 85% of the bottom of
439 the ionosphere. In (Jacobson et al., 2018) it was found that most lightning strokes were not
440 detected by the C/NOFS instruments, while occasionally there was greatly enhanced
441 transmission of LG waves to the satellite. Quantitatively, from line 6 of table 1 of (Jacobson et
442 al., 2018) listing a population of 136-thousand WWLLN strokes having predicted strong
443 Poynting vector fluence at the subsatellite point, the estimated number of coincident Vector
444 Electric Field Investigation (VEFI) whistlers, from line 13 of table 1 was only 19-thousand
445 (14%). These authors suggested that km-scale D-layer irregularities might be responsible for
446 these effects. Frequently appearing foamy plasma bubble roots of the sort discussed here in
447 connection with Figure **8** could explain both the lack of detection for most lightning strokes
448 noted by (Jacobson et al., 2018) and the occasional greatly enhanced transmission. The rare
449 enhanced transmission observations would correspond to cases for which the C/NOFS satellite
450 was either immersed in, or just above, a plasma bubble root, while the more common lack of
451 detection would correspond to foamy, strongly attenuating bubbles not extending up to the
452 C/NOFS satellite that effectively absorbed most of the LG energy. Despite the quite different
453 analysis approaches of (Zheng et al., 2015) and (Jacobson et al., 2018), their coincident rates
454 between satellite observations of whistlers and WWLLN detected lightning strokes are in
455 reasonable agreement.

456 In conclusion, it is suggested that most (~80%) of the bottom of the nocturnal equatorial
457 ionosphere is covered with a "foamy" layer of plasma bubbles that extend contiguously down to
458 neutral atmosphere. Whether this foam is turbulent is an open question. The detailed spatial
459 structure of this foam is an open question. The possibility of two-phase foamy structure at the
460 base of the ionosphere may complicate theoretical analyses that implicitly assume a single-phase
461 medium. Many other such questions remain open, but it is hoped that follow up observations and
462 theoretical analysis might be stimulated by the present suggestions.

463 **Acknowledgments**

472 **Open Research**

473 Van Allen Probe data used in this paper can be found in the EMFISIS archive
474 (http://emfisis.physics.uiowa.edu/data/index). In this index file, descriptions of each of the
475 relevant data sets, including the file naming format, are provided. The specific level 2 data
476 products involved in the present work include the "WFR-waveform-continuous-burst_emfisis-

477 L2", "WFR-spectral-matrix-diagonal_emfisis-L2", "magnetometer_uvw_emfisis-L2". The
478 specific level 3 data products are "magnetometer_hires-geo_emfisis-L3". Swarm data used in
479 this paper is provided by the European Space Agency and can be accessed online at
480 https://swarm-diss.eo.esa.int. The high rate VFM data was taken from the level 1b
481 "latest_baselines" folder containing "MACx_HR" files for each of the three Swarm satellites.
482 WERA data used in this paper is described in detail on the WERA project website:
483 http://www.oa.uj.edu.pl/elf/index/projects3.htm and may be freely available for scientific
484 analysis by contacting the WERA personnel. WWLLN data was purchased from the University
485 of Washington (https://wwlln.net). GLM data is available at no cost from the Geostationary
486 Operational Environmental Satellites-R Series web site (https://www.goes-r.gov), but the user
487 must register to obtain the GOES-R Series GLM L2+ Data Product "GRGLMPROD" and must
488 select an appropriate time range for data access on the web-page:
489 https://www.avl.class.noaa.gov/saa/products/search?datatype_family=GRGLMPROD.
490

References

492 Abarca, S.F., Corbosiero, K.L., & Galarneau, T.J. Jr. (2010). An evaluation of the Worldwide
493   Lightning Location Network (WWLLN) using the National Lightning Detection Network
494   (NLDN) as ground truth. *Journal of Geophysical Research, 15*, D18206,
495   doi:10.1029/2009JD013411
496 Abdu, M.A., Batista, I.S., Reinisch, B.W., MacDougall, J.W., Kherani, E.A., & Sobral, H.H.A
497   (2012). Equatorial range spread F echoes from coherent backscatter, and irregularity
498   growth processes, from conjugate point digital ionograms., *Radio Science*, 47, RS6003,
499   doi:10.1029/2012RS005002
500 Akhtar, N, Hussain, S., & Mahmood, S. (2021). Nonlinear propagation of fast and slow
501   magnetosonic waves in collisional plasmas. *Contributions to Plasma Physics*.
502   https://doi.org/10.1002/ctpp.202000210
503 Balan, N., Liu, LiBo & Le, H. (2018). A brief review of equatorial ionization anomaly and
504   ionospheric irregularities. *Earth and Planetary Physics, 2*, 257-275,
505   https://doi.org/10.26464/epp2018025
506 Bateman, M., Mach, D., & Stock, M. (2020). Further investigation into detection efficiency and
507   false alarm rate for the geostationary lightning mappers aboard GOES-16 and GOES-17.
508   *Earth and Space Science, 8*, 2020EA001237. https://doi.org/2020EA001237
509 Benjelloun, S. & Ghidaglia, J.-M. (2021). On the sound speed in two-fluid mixtures and the
510   implications for CFD model validation. European Journal of Mechanics / B Fluids, 90,
511   152-168. https://doi.org/10.1016/j.euromechflu.2021.09.002
512 Bennett, C.L. (2023). A Novel Population of Slow Magnetosonic Waves and a Method for the
513   Observation of the Roots of Plasma Bubbles in the Lower Ionosphere. *ESS Open Archive*.
514   January 17, 2023, doi:10.1002/essoar.10511954.3
515 Chou, M.Y., Yue, J., Sassi, F., Huba, J., McDonald, S.E., Tate, J.L., et al, (2022). Modeling the
516   Day-to-Day Variability of Midnight Equatorial Plasma Bubbles with SAMI3/WACCM-
517   X. Authorea. December 27, 2022, doi:10.22541/essoar.167214177.74303978/v1
518 De Jonghe, J. & Keppens, R. (2020a). A two-fluid analysis of waves in a warm ion-electron
519   plasma. *Plys. Plasmas*. *27*, 122107, doi:10.1063/5.0029534

520   De Jonghe, J. & Keppens, R. (2020b). Two-Fluid Treatment of Whistling Behavior and the
521   Warm Appleton-Hartree Extension. *Journal of Geophysical Research: Space Physics,*
522   *126,* e2020JA028953, doi:10.1029/2020JA028953
523   De Michelis, P., Consolini, G., Alberti, T., Tozzi, R., Giannattasio, F., Coco, I., et al. (2022).
524   Magnetic Field and Electron Density Scaling Properties in the Equatorial Plasma
525   Bubbles. *Remote Sens. 14*, 918, doi:10.3390/rs14040918
526   De Michelis, P., Consolini, G., Tozzi, R., Pignalberi, A., Pezzopane, M., Coco, I., et al. (2021).
527   Ionospheric Turbulence and the Equatorial Plasma Density Irregularities: Scaling
528   Features and RODI. *Remote Sens. 13*, 759, doi:10.3390/rs13040759
529   Elias, F., Crassous, J., Derec, C., Dollet, B., Drenckhan, W., Gay, C., et al. (2020). The
530   Acoustics of Liquid Foams, *Current Opinion in Colloid & Interface Science, 50*, 10139,
531   doi:10.1016/j.cocis.2020.101391
532   Golkowski, M., Sarker, S.R., Renick, C., Moore, R.C., Cohen, M.B., Kulak, A., Mlyanarczyk, J.,
533   & Kubisz, J. (2018). Ionospheric D Region Remote Sensing Using ELF Sferic Group
534   Velocity. *Geophysical Research Letters, 45*, 12,739-12,748, doi:10.1029/2018GL080108
535   Goodman, S., Blakeslee, R., Koshak, W., Mach, D., Bailey, J., Buechler, D., et al. (2013). The
536   goes-r Geostationary Lightning Mapper (GLM). *Atmospheric Research, 125-126*, 34-49,
537   doi:10.1016/j.atmosres.2013.01.006
538   Goodman, S., Mach, D., Koshak, W., Blakeslee, R. (2012). Algorithm theoretical basis
539   document: GLM lightning cluster-filter algorithm. Version 3.0. July 30, 2012. NOAA
540   NESDIS Center for satellite applications research.
541   Heelis, R. (2004). Electrodynamics in the low and middle latitude ionosphere: A tutorial. *Journal
542   of Atmospheric and Solar-Terrestrial Physics, 66*(10), 825-838,
543   doi:10.1016/j.jastp.2004.01.034
544   Holzworth, R.H., McCarthy, M.P., Brundell, J.B., Jacobson, A.R. & Rodger, C.J. (2019). Global
545   distribution of superbolts. *Journal of Geophysical Research: Atmospheres, 124*, 9996-
546   10,005, doi:10.1029/2019JD030975
547   Huba, J.D. (2023). Resolution of the equatorial spread F problem: Revisited. *Front. Astron.
548   Space Sci.* 9:1098083, doi:10.3389/fspas.2022.1098083
549   Hutchins, M.L., Holzworth, R.H., Rodger, C.J., & Brundell, J.B. (2012). Far-field power of
550   lightning strokes as measured by the world-wide lightning location network. *Journal of
551   Atmospheric and Oceanic Technology, 29*, 1102-1110. https://doi.org/10.1175/JTECH-D-
552   11-00174.1
553   Hysell, D.L., Larsen, M.F., Swenson, C.M., Barjatya, A., Wheeler, T.F., Sarango, M.F., et al.
554   (2005). Onset conditions for equatorial spread F determined during EQUIS II.
555   *Geophysical Research Letters*, *32* (L24104), doi:10.1029/2005GL024743
556   Immel, T.J., Mende, S.B., Frey, H.U., Peticolas, L.M., & Sagawa, E. (2003). Determination of
557   low latitude plasma drifts speeds from FUV images. *Geophysical Research Letters,
558   30*(18), 1945, doi:10.1029/2003GL017573
559   Jackson, J.D. (1975). *Classical Electrodynamics.* New York: John Wiley & Sons.
560   Jacobson, A.R., Holzworth, R.H., Pfaff, R. & Roderick H. (2018). Coordinated Satellite
561   Observations of the Very Low Frequency Transmission Through the Ionospheric D Layer
562   at Low Latitudes, Using Broadband Radio Emissions from Lightning. *Journal of
563   Geophysical Research: Space Physics, 123*, 2926-2952, doi:10.1002/2017JA024942
564   Kelley, M.C., Makela, J.J., de La Beaujardiere, O., & Retterer, J. (2011). Convective Ionospheric
565   Storms: A Review. *Rev. Geophys., 49*, RG2003, doi:10.1029/2010RG000340

Karan, D.K., Daniell, R.E., England, S.L., Martinis, C.R., Eastes, R.W., Burns, A.G., & McClintock, W.E. (2020). First zonal drift velocity measurement of equatorial plasma bubbles (EPBs) from a geostationary orbit using GOLD data. *Journal of Geophysics: Space Physics 125*, e2020JA028173, doi:10.1029/2020JA028173

Kil, H., Demajistre, R., & Paxton, L.J. (2004). F-region plasma distribution seen from TIMED/GUVI and its relation to the equatorial spread F activity. *Journal of Geophysical Research, 31*, L05810, doi:10.1029/2003GL018703

Kil, H., & Heelis, R.A. (1998). Global distribution of density irregularities in the equatorial ionosphere. *Journal of Geophysical Research, 103*, 407-417 doi:10.1029/97JA02698

Kil, H., Sun, K.A., Chang, H., Paxton, L.J., Nikoukar, R., & Lee, J. (2022). Characteristics and sources of electron density irregularities near and after midnight in the equatorial F region. Oral presentation SA55A-03 at AGU fall meeting, Chicago Illinois, USA. https://agu.confex.com/agu/fm22/meetingapp.cgi/Paper/1177560

Kudeki, E., & Bhattacharyya, S. (1999). Postsunset vortex in equatorial F-region plasma drifts and implications for bottomside spread F. *Journal of Geophysical Research*, 104(A12), 28, 163-28, 170, doi:10.1029/1998JA900111

Liang, J., Donovan, E., Jackel, B., Spanswick, E. & Gillies, M. (2016) On the 630 nm red-line pulsating aurora: Red-line Emission Geospace Observatory observations and model simulations. *Journal of Geophysical Research: Space Physics, 121*, 79880-8012, doi:10.1002/2016JA022901

Makela, J.J., & Kelley, M.C. (2003). Field-aligned 777.4-nm composite airglow images of equatorial plasma depletions. *Geophysical Research Letters, 30*(8), 1442, doi:10.1029/2003GL017106

Makela, J.J., Kelley, M.C., & Nicolls, M.J. (2006). Optical observations of the development of secondary instabilities on the eastern wall of an equatorial plasma bubble, *J. Geophys. Res., 111*, A09311, doi:10.1029/2006JA011646

Makela, J.J. & Miller, E.S. (2008). Optical observations of the growth and day-to-day variability of equatorial plasma bubbles, *J. Geophys. Res., 113*, A03307, doi:10.1029/2007JA012661

Makela, J.J. & Otsuka, Y. (2012). Overview of Nighttime Ionospheric Instabilities at Low- and Mid-Latitudes: Coupling Aspects Resulting in Structuring at the Mesoscale. *Space Sci. Rev 168*, 419-440, doi:10.1007/s11214-011-9816-6

Martinis, C., Eccles, J.V., Baumgardner, J., Manzano, J., & Mendillo, M. (2003). Latitude dependence of zonal plasma drifts obtained from dual-site airglow observations. *Journal of Geophysical Research, 108*(A3), 1129, doi:10.1029/2002JA009462

Mendillo, M., & Baumgardner, J. (1982). Airglow characteristics of equatorial plasma depletions. *Journal of Geophysical Research, 87*(A9), 7641-7652, doi:10.1029/JA087iA09p07641

Min, K., Takahashi, K., Ukhorskiy, A.Y., Manweiler, J.W., Spence, H.E., Singer, H.J., et al. (2017), Second harmonic poloidal waves observed by Van Allen Probes in the dusk-midnight sector. *J. Geophys. Res. Space Physics, 122*, 3013-3039, doi:10.1002/2016JA023770

Narayanan, V.L., Sau, S., Gurubaran, S., Shiokawa, K., Balan, N., & Emperumal, K. (2014). A statistical study of satellite traces and subsequent evolution of equatorial spread F based on ionosonde observations over dip equatorial site Tirunelveli, India. *Earth, Planets and Space*, 676(1), 160, doi:10.1186/s40623-014-0160-4

Nickolaenko, A.P., & Rabinowicz, L.M. (2004). Time domain presentation for ELF pusles with accelerated convergence. *Geophysical Research Letters, 31*, L05808, doi:10.1029/2003GL018700

Patra, A.K., Yokoyama, T., Yamamoto, M., Saito, S., Maruyama, T. & Fukao, S. (2005). Disruption of E region echoes observed by the EAR during the development phase of equatorial spread F: A manifestation of electrostatic field coupling. *Geophysical Research Letters, 32*(L17104), doi:10.29/2005GL022868

Pierre, J., Guillermic, R., Elias, R., Drenckhan, W., & Leroy, V. (2013). Acoustic characterization of liquid foams with an impedance tube. *The European Physical Journal E 36*(113), doi:10.1140/epje/i2013-13113-1

Piggott, W.R. & Rawer, K. (1972). URSI Handbook of Ionogram Interpretation and Reduction, second Edition, Novermber 1972, WDC A, Report UAG-23. https://repository.library.noaa.gov/view/noaa/10404

Pimenta, A.A., Bittencourt, J.A., Fagundes, P.R., Sahai, Y., Buriti, R.A., Takahashi, H., & Taylor, M.J. (2003). Ionospheric plasma bubble zonal drifts over the tropical region: A study using OI 630 nm emission all-sky images. *Journal of Atmospheric and Solar-Terrestrial Physics, 65*(10), 1117-1126, doi:10.1016/S1364-6826(03)00149-4

Ripoll, J.F., Farges, T., Malaspina, D.M., Lay, E.H., Cunningham, G.S., Hospodarsky, G.B. et al. (2020), Analysis of Electric and Magnetic Lightning-Generated Wave Amplitudes Measured by the Van Allen Probes. *Geophysical Research Letters, 47*, e2020GL087503, doi:10.1029/2020GL087503

Ritter, P., Luhr, H., & Rauberg, J. (2013), Determining field-aligned currents with the Swarm constellation mission. *Earth Planets Space, 65*, 1285-1294, doi:10.5047/eps.2013.09.006

Rodriguez-Zuluaga, J., Stolle, C., Yamazaki, Y., Xiong, C., & England, S.L. (2020). A synoptic-scale wavelike structure in the nighttime equatorial ionization anomaly. *Earth and Space Science, 8*, e2020EA001529, doi:10.1029/2020EA001529

Rudlosky, S., Goodman, S., Virts, K., & Bruning, E. (2019). Initial Geostationary Lightning Mapper observations. *Geophysical Research Letters, 46*, 1097-1104, doi:10.1029/2018GL081052

Santolik, O., Parrot, M., & Lefeuvre, F. (2003). Singular value decomposition methods for wave propagation analysis. *Radio Science, 38*(1), 1010, doi:10.1029/2000RS002523

Shiokawa, K., Otsuka, Y., Ogawa, T., & Wilkinson, P. (2004). Time evolution of high-altitude plasma bubbles imaged at geomagnetic conjugate points. *Annales Geophysicae, 29*(9), 3137-3143, doi:10.5194/angeo-22-3137-2004

Sivakandan, M., Mondal, S., Sarkhel, S., Chakrabarty, D., Sunil Krishna, M., V. Upadhayaya, A.K., et al. (2021). Evidence for the in-situ generation of plasma depletion structures over the transition region of geomagnetic low-mid latitude. *Journal of Geophysical Research: Space Physics, 126*, e2020JA028837, doi:10.1029/2020JA028837

Tsunoda, R.T. (1983). On the generation and growth of equatorial backscatter plumes: 2. Structuring of the west walls of upwellings. *Geophysical Research Letters, 88*(A6), 4869-4874, doi:10.1029/JA088iA06p04869

Wood, A.B. (1941). Textbook of Sound: Being an Account of the Physics of Vibrations with Special Reference to Recent Theoretical and Technical Developments, Second Edition, page 361, Macmillan Co., New York.

Woodman, R.F. (2009). Spread F - an old equatorial aeronomy problem finally resolved? *Ann. Geophysics 27*(5), 1915-1934, doi:10.5194/angeo-27-1915-2009

658   Woodman, R.F. and Hoz, C.L. Radar Observations of F Region Equatorial Irregularities. *Journal*
659   *of Geophysical Research, 81*(31), 5447-5466, doi:10.1029/JA081i031p05447
660   Yokoyama, T., Yamamoto, M., Otsuka, Y., Nishioka, M., Tsugawa, T., Watanabe, S., & Pfaff,
661   R.F. (2011). On postmidnight low-latitude ionospheric irregularities during solar
662   minimum: 1. Equatorial Atmosphere Radar and GPS-TEC observations in Indonesia.
663   *Journal of Geophysical Research, 116*, A11325, doi:10.1029/2011JA016797
664   Zheng, H., Holzworth, R.H., Brundell, J.B., Jacobson, A.R., Wygant, J.R., Hospodarsky, G.B.,
665   Mozer, F.S., & Bonnell, J. (2015). A statistical study of whistler waves observed by Van
666   Allen Probes (RBSP) and lightning detected by WWLLN. *Journal of Geophysical*
667   *Research: Space Physics, 121*, 2067-2079, doi:10.1002/2015JA022010

668
669

670   **Figure 1.** Scalograms (in **a**, **c**, and **e**) and time resolved plots (**b**, **d**, and **f**) of the electric field
671   components are shown for a period while VAP-A passes through the root of a plasma bubble. In
672   (**g**) the summation of the radial electric field contributions from all WWLLN detected lightning
673   strokes within this time interval using the (Nickolaenko et al., 2004) model with WWLLN
674   determined amplitudes is plotted. The percentage values shown above the three peaks in **f**
675   represent the ratios of the observed peak amplitudes to the model amplitudes of the
676   corresponding peaks seen in (**g**). The predicted arrival times at the subsatellite location using
677   WWLLN/GLM stroke times are shown by the red/white dashed vertical lines in (**a**, **c** and **e**). The
678   GLM times appear systematically later by 2 ms than the WWLLN times. The second of the
679   peaks in (**f**) was seen by GLM but not detected by WWLLN. In the scalograms, some extraneous
680   radio frequency interference at approximately 2 kHz and harmonics can be seen. The geographic
681   location of the subsatellite point at the start of this data burst is shown in the title. Also shown is
682   the location of the flash responsible for the four peaks in (**f**). The angular difference between
683   these locations along the great circle is shown as $\Delta\theta$.

684

685   **Figure 2.** Scalograms and time resolved plots of VAP-A data with the same layout as in the
686   previous figure are shown for a different period. The percentage values shown above the three
687   peaks in (**f**) represent the ratios of the observed peak amplitudes to the model amplitudes of the
688   corresponding peaks seen in (**g**). As in the previous figure, and in similar subsequent figures, the
689   angular distance along the great circle containing both the satellite location and the relevant
690   lightning flash location is indicated by the value of $\Delta\theta$ in the figure title.

691

Figure 3. Scalograms of the three magnetic and electric field components in the spinning U,V, W reference frame are displayed for a 1.6 s sample of EMFISIS data. The dashed line curves represent four distinct dispersion constant (DC) values that track the dispersed waves from a single lighting stroke detected by the WWLLN. In (**a**, **b** and **c**), scalograms for the Bu, Bv and Bw components of the magnetic field are shown. In **d**, **e** and **f**, scalograms for the Eu, Ev and Ew components of the electric field are shown. The approximate location and local solar time (LST) of the satellite at the time of this data collection is shown in the figure title.

Figure 4. The direction and speed for four different DC values are displayed for points along each of the dispersion curves shown in the previous figure. In (**a**, **f**, **k** and **p**), the absolute values for the projections of the Poynting unit vector **S** along μ (the direction of the local magnetic field **B**) are plotted as a function of frequency. Similarly in (**b**, **g**, **l** and **q**), projections along the ν direction (approximately vertical) of the MFA coordinate system are shown. Also similarly in (**c**, **h**, **m** and **r**), projections along the ϕ direction (magnetic East) of the MFA coordinate system are shown. In (**d**, **i**, **n**, **s**), the magnitudes of the electric and magnetic field amplitudes are shown as a function of frequency. In (**e**, **j**, **o**, and **t**) the RPA estimated phase velocities are plotted as a function of frequency.

Figure 5. Scalograms of the three magnetic and electric field components in the spinning U,V, W reference frame are displayed for a single burst of EMFISIS data. The white dashed vertical lines are plotted at the times of the arrival at the subsatellite location for every WWLLN event detected during this data burst. In (**a**, **b** and **c**), scalograms for the Bu, Bv and Bw components of the magnetic field are shown. In (**d**, **e** and **f**), scalograms for the Eu, Ev and Ew components of the electric field are shown. In (**g**), the satellite spin vector coordinates λ (in the fashion of latitude) and δ (in the fashion of longitude), characterizing the spin vector orientation relative to the local magnetic field, are indicated over the course of this data burst. The approximate location and local solar time (LST) of the satellite at the start of this data burst is shown in the legend for section (**g**).

Figure 6. Scalograms for the indicated subset of the time range in the previous figure are shown here. In (**a**, **b** and **c**), scalograms of the three magnetic field components are shown. In (**d**, **e** and **f**), scalograms of the three electric field components are shown. In (**f**), the arc distances, (80°, 18°, 162° and 79°), along the great circle containing the subsatellite location and the four WWLLN stroke locations are shown in blue text labels near the four dashed red vertical lines for the estimated arrival times at the subsatellite location of the four WWLLN strokes. The first two strokes appear sufficiently isolated that they may be tentatively identified with the scalogram spikes labelled #1 and #2 in (**f**).

728   **Figure 7**. A wavevector analysis with the same layout as that displayed in Figure **4** is shown here
729   for the four times indicated in Figure (**6f**) by white vertical dashed lines and numbered #3, #4, #5
730   and #8. The locally dispersionless nature of the scalogram peaks seen in Figure 6 is validated by
731   the nearly constant phase velocity values above the local Oxygen cyclotron frequency seen
732   especially clearly in (**e** and **o**).

733   **Figure 8**. A physical model of a region of "foamy plasma" near the bottom of the ionosphere is
734   illustrated. A sketch of the "Wood's law" derivation of the estimated speed of sound in the two-
735   phase mixture is shown.

736   **Figure 9**. The variation of dispersionless pulse attenuation as a function of propagation delay
737   through foamy plasma is plotted. The two points with error bars shown represent the two cases
738   displayed in Figures **1** and **2** above.
739

Figure 1.

Viewpoint: -2.5°N -154.6°E Alt 238.6km V(EIWG)= 245 km/s Single Flash 4 Strokes @ 9.2°N 84.8°W Δθ=71°
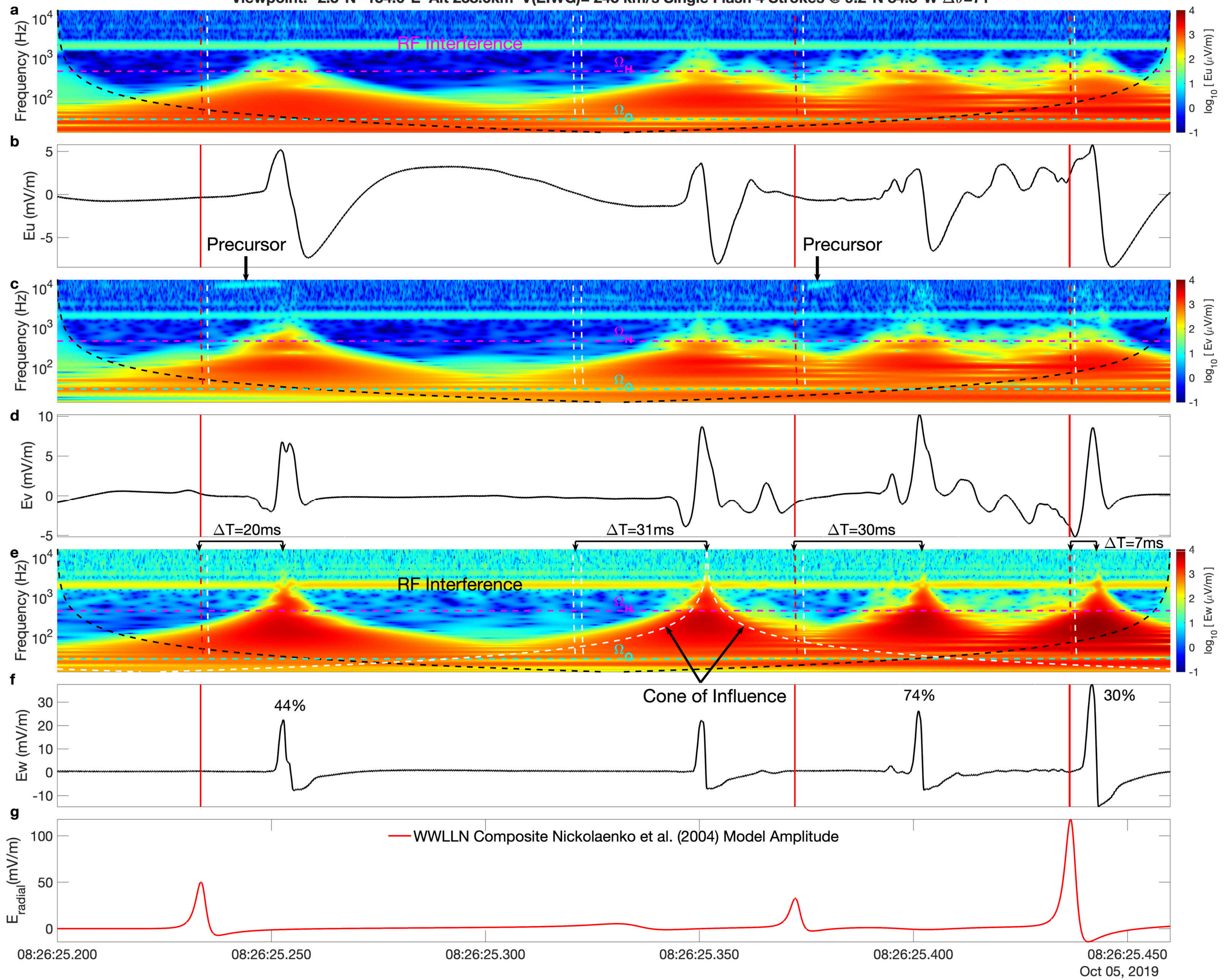
Figure 2.

Viewpoint: -4.7°N -165.9°E Alt 241.9km V(ElWG)= 245 km/s Single Flash 3 Strokes @ 12.7°N 152.8°E Δθ=45°

Figure 3.

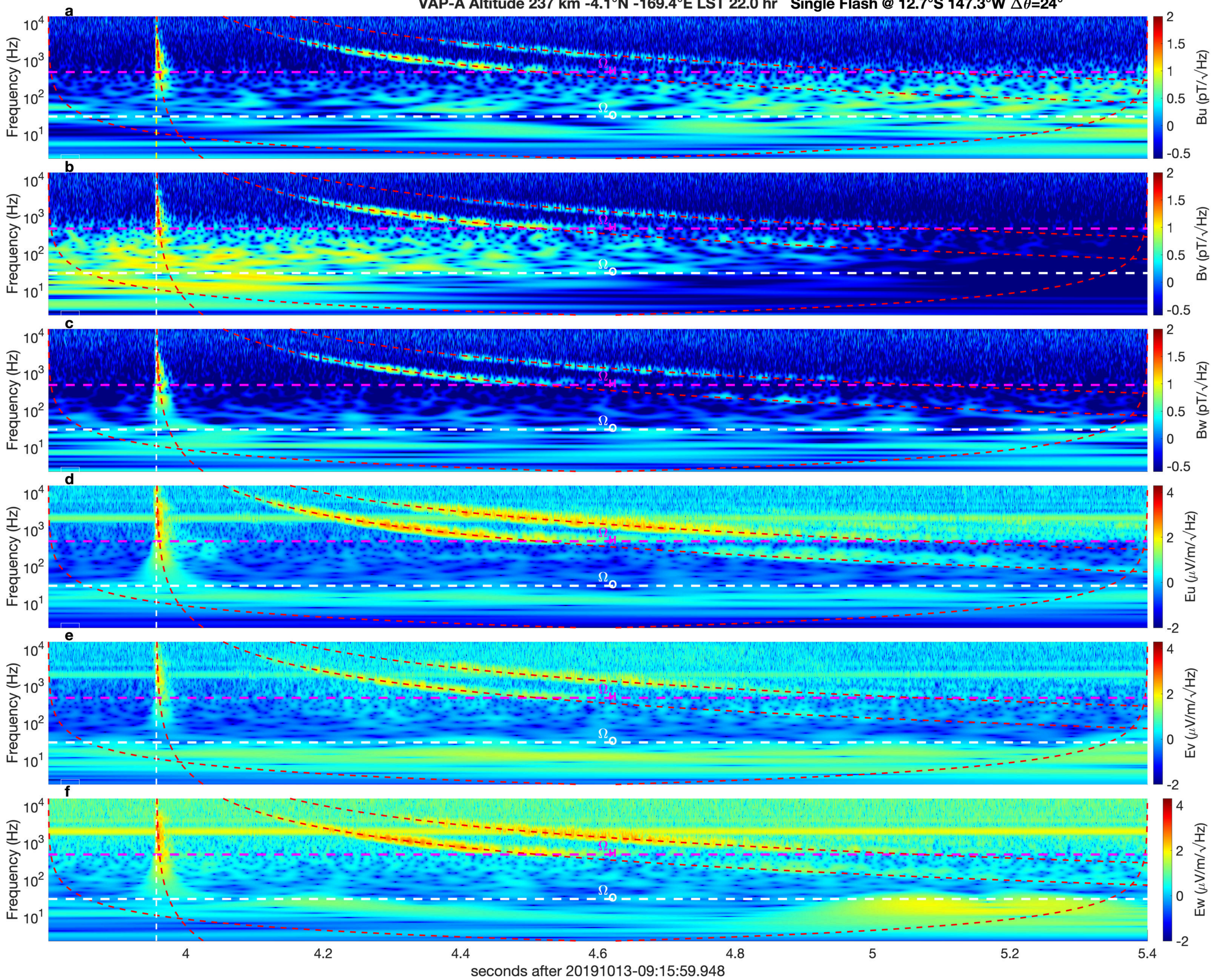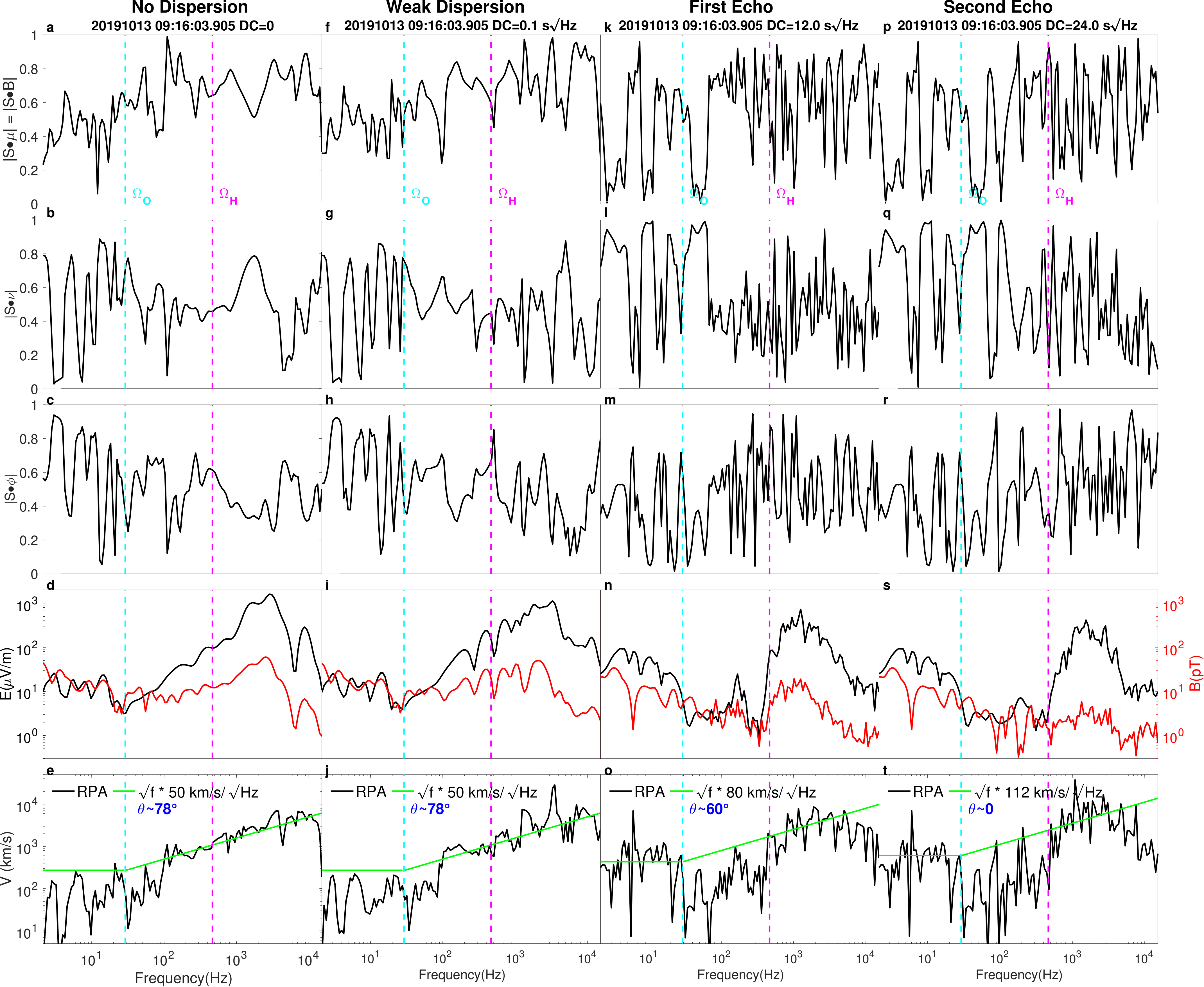VAP-A Altitude 237 km -4.1°N -169.4°E LST 22.0 hr   Single Flash @ 12.7°S 147.3°W Δθ=24°
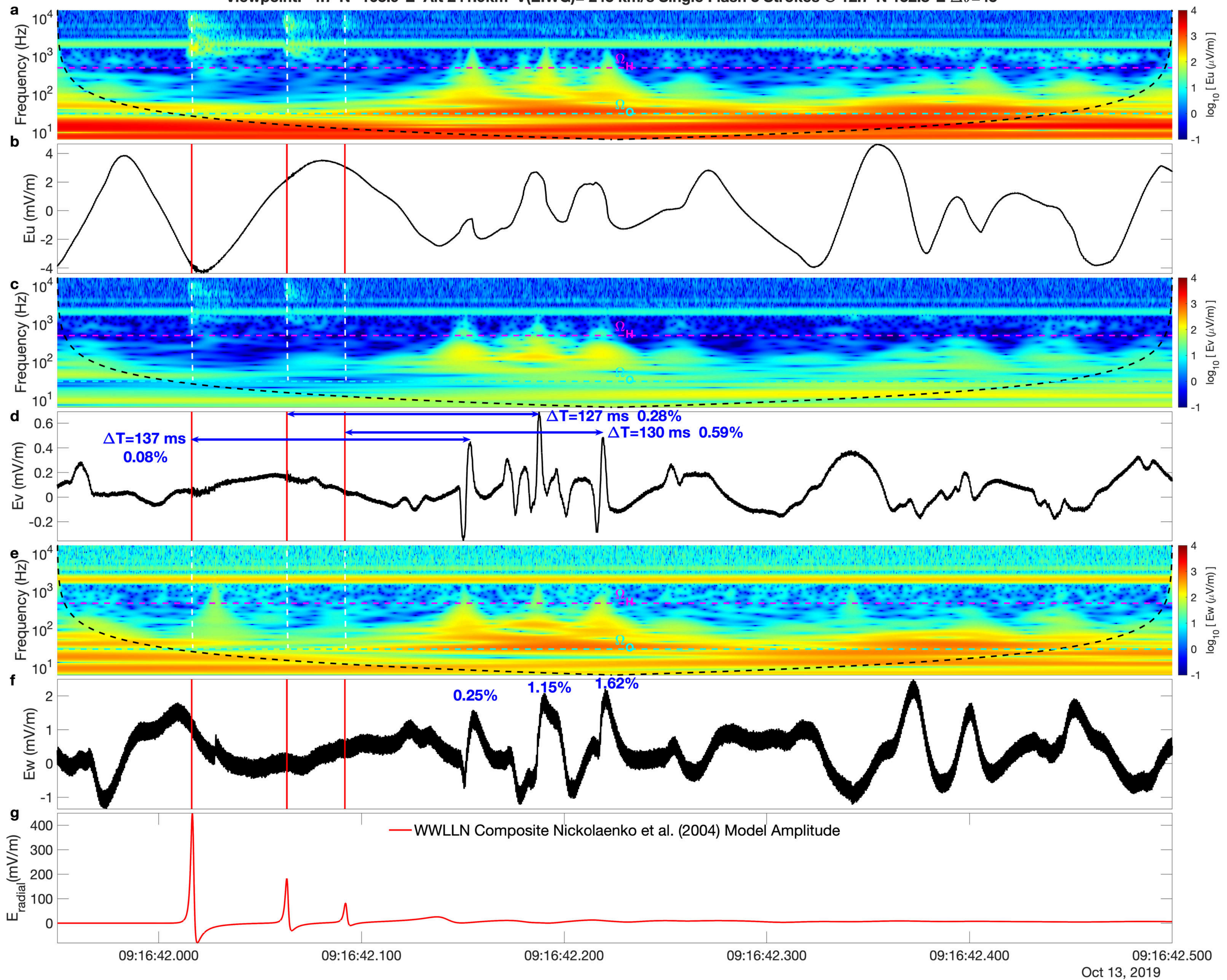
Figure 4.

Figure 5.

Magnetic & Electric Field Scalograms

Alt=269km Speed=9.6km/s Lat=-1.41°N Lon=199.0°E |B|=28.81 μT LST=21.68hr

cos(λ) (1 => U)   sin(δ) (1 => W) − − 0

Period of Interest

Oct 05, 2019

Figure 6.

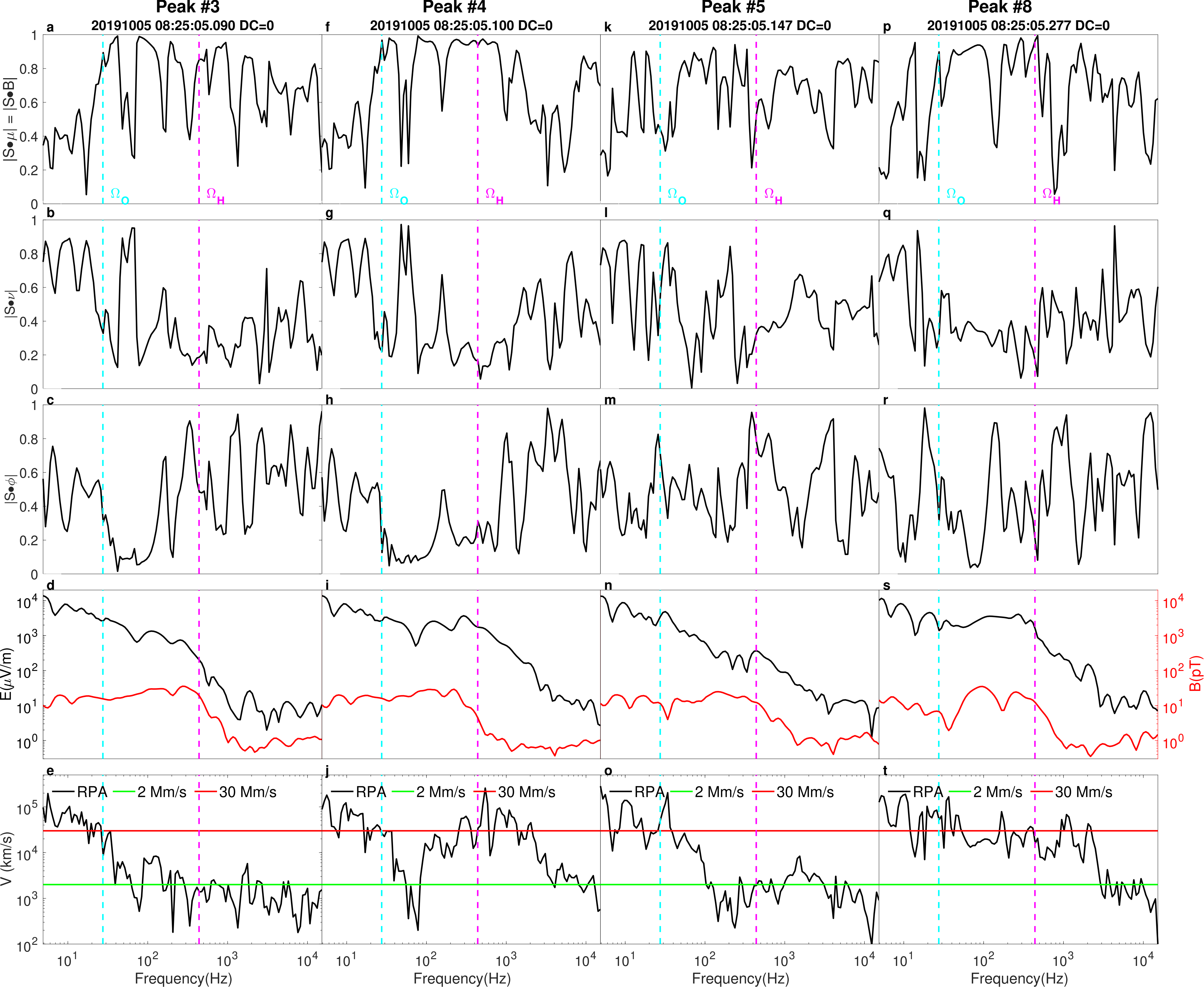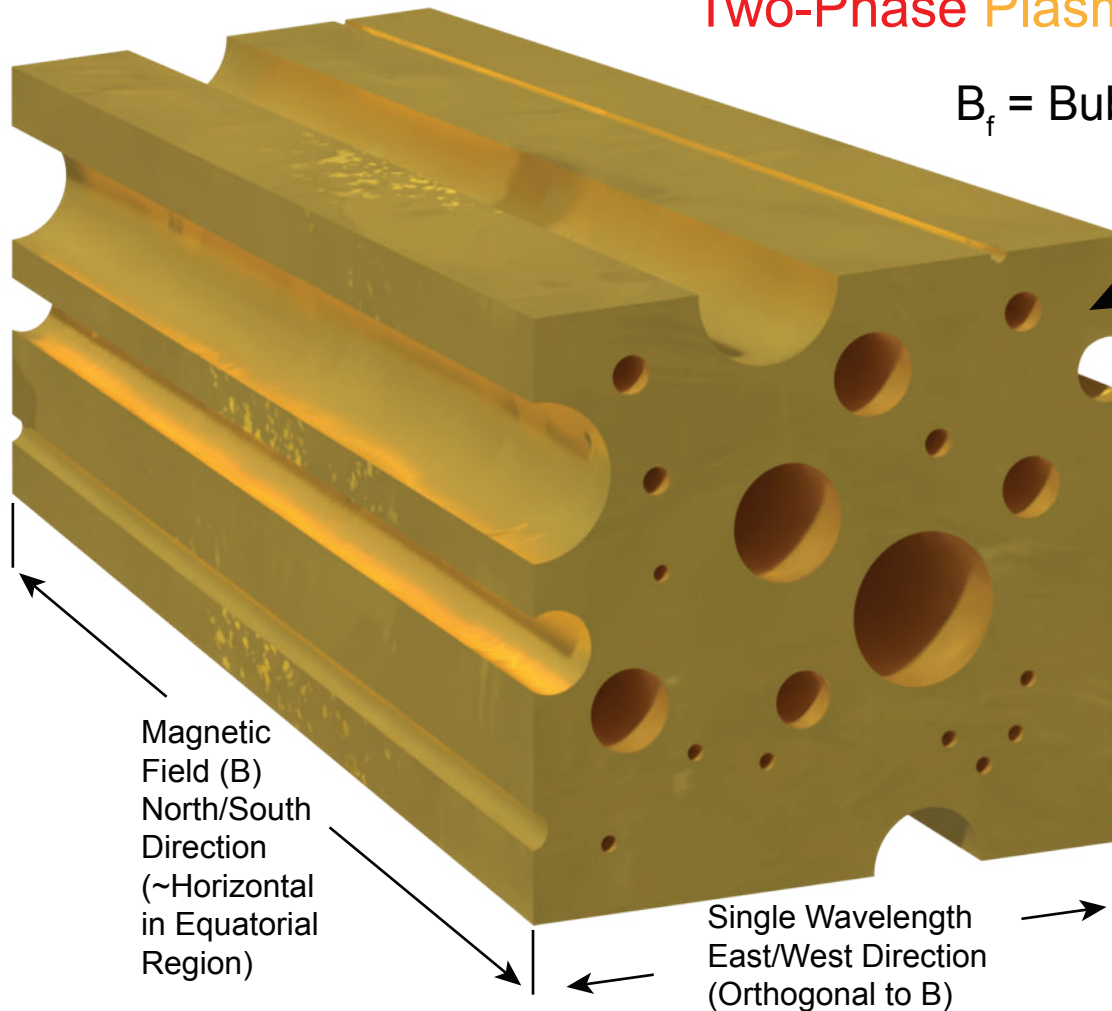VAP-A Altitude 269 km -1.4°N -161.0°E LST 21.7 hr
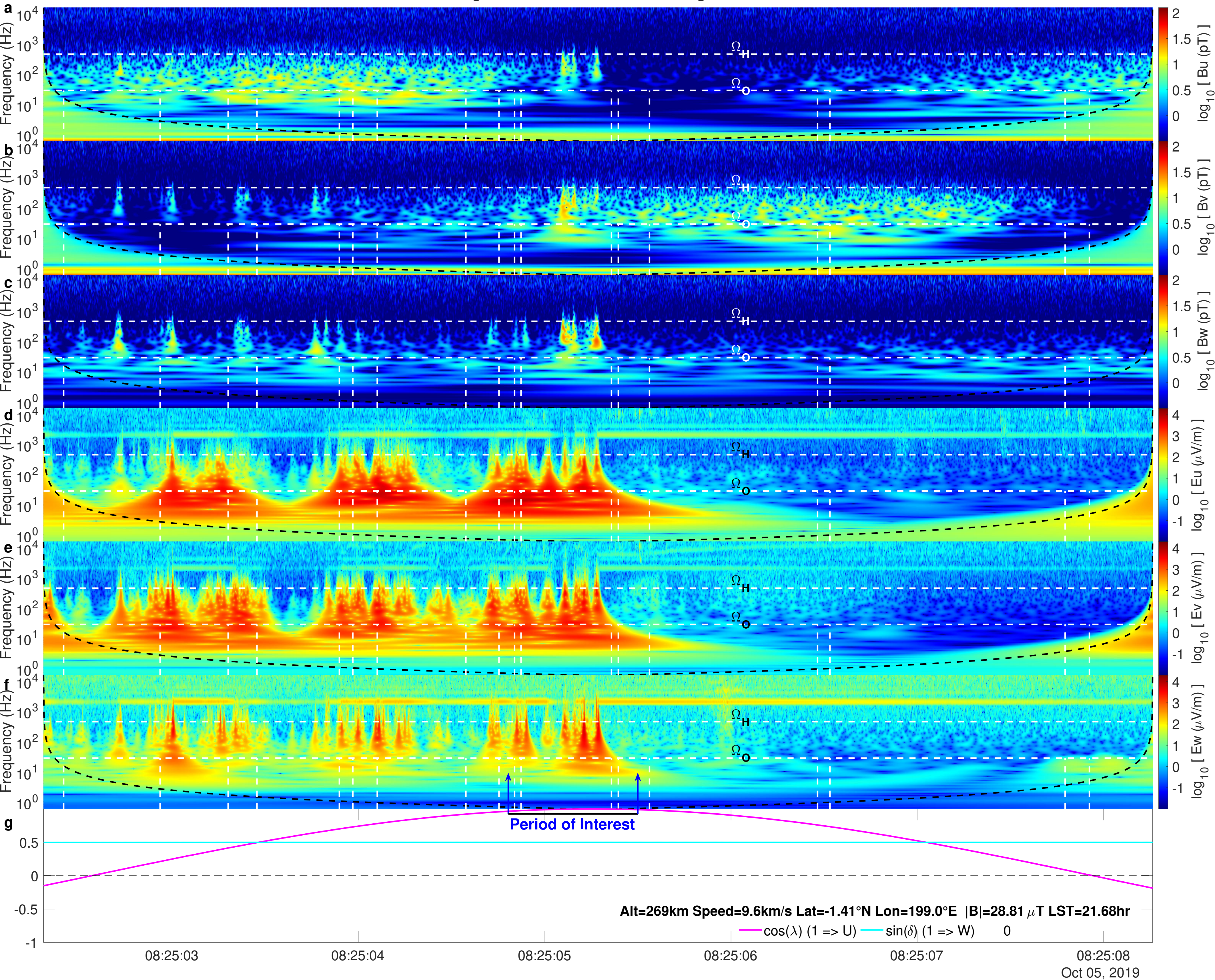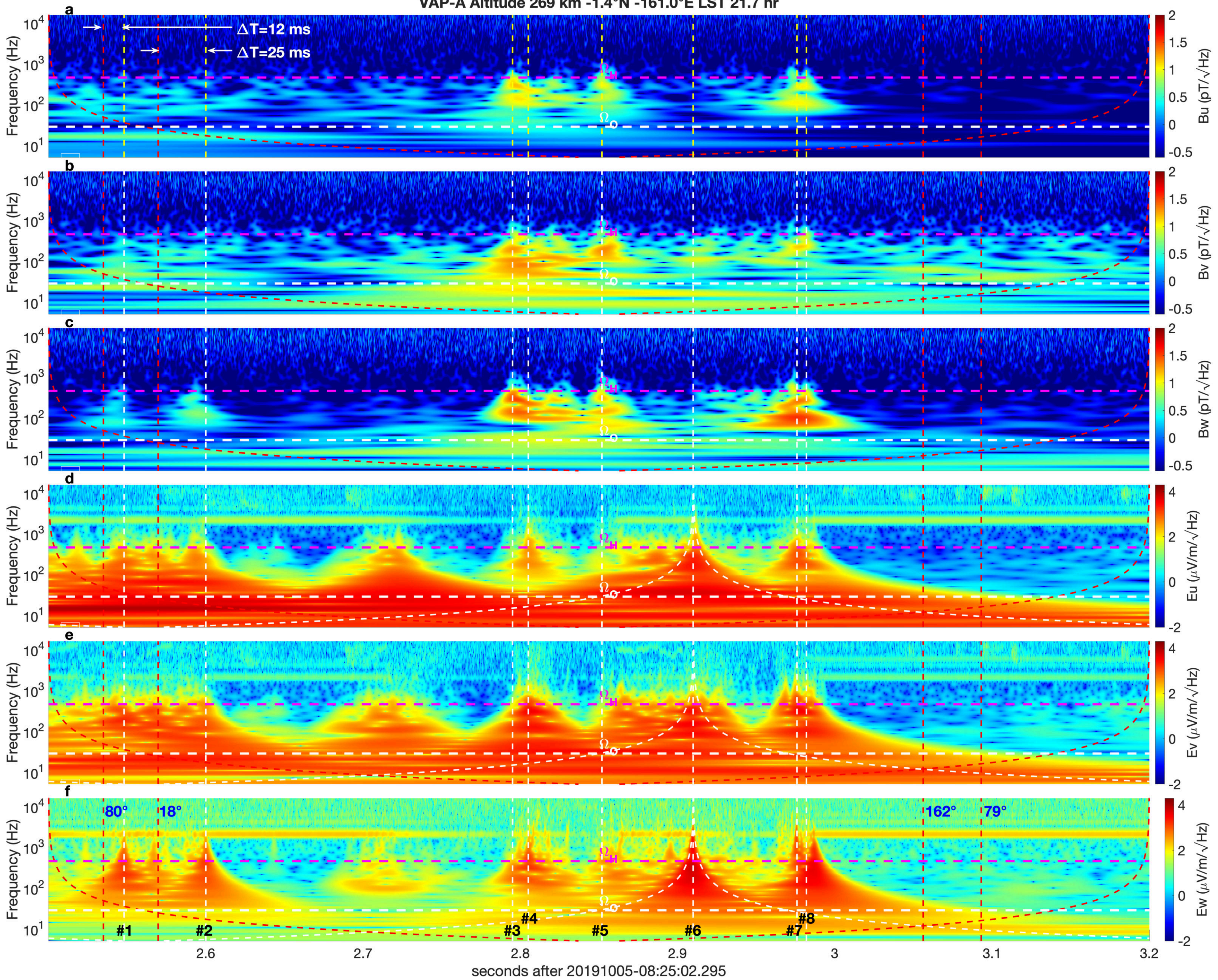
Figure 7.

Figure 8.

Speed of Sound in "Foamy" Two-Phase Plasma/Bubble Mix

B_f = Bubble Volume Fraction

Densities
$$\rho_{Plasma} \gg \rho_{Bubble}$$

Compressibilities
$$\chi_{Plasma} \ll \chi_{Bubble}$$

Mixture Density
$$\rho_{Mix} = (1-B_f)\,\rho_{Plasma} + B_f\,\rho_{Bubble}$$

Mixture Compressibility
$$\chi_{Mix} = (1-B_f)\,\chi_{Plasma} + B_f\,\chi_{Bubble}$$

Magnetic Field (B) North/South Direction (~Horizontal in Equatorial Region)

Single Wavelength East/West Direction (Orthogonal to B)

$$V_{Mix} = \frac{1}{\sqrt{\rho_{Mix}\,\chi_{Mix}}} \approx \frac{1}{\sqrt{(1-B_f)\,B_f\,\rho_{Plasma}\,\chi_{Bubble}}} < V_{Plasma} \;\; \& \;\; < V_{Bubble}$$

"Wood's Law"

Figure 9.